RESEARCH ARTICLE

annalen der physik
www.ann-phys.org

Nonlinear Dynamics of the Photonic Spin Hall Effect in Rydberg Atoms

Muqaddar Abbas, Wenzhang Liu, Pei Zhang, and Hamid R. Hamedi**

The photonic spin Hall effect (SHE) is explored in a highly tunable Rydberg-based atomic system by leveraging the distinctive properties of Rydberg superatoms. These superatoms arise from strong dipole–dipole interactions and extended radiative lifetimes, resulting in collective excitations governed by the dipole blockade mechanism. An ensemble of three-level atoms in a cascade configuration models a medium in which each superatom acts as a coherent quantum entity. The photonic SHE shows strong dependence on the probe field Rabi frequency and atomic number density. At high Rabi frequencies, the blockade effect suppresses the photonic SHE, confining its occurrence to specific resonant conditions. In contrast, under weak probe excitation, the blockade influence diminishes, enabling an amplified photonic SHE response at resonant detuning due to increased light-matter interaction sensitivity. Reducing atomic number density further broadens the detuning range over which the photonic SHE occurs, indicating a transition toward a more sensitive, less resonance-constrained optical behavior. The effect of van der Waals interactions on the photonic SHE shift is also characterized. This expanded operational bandwidth demonstrates the potential of Rydberg-based systems for robust spin-optical control, particularly in scenarios where precise stabilization of the probe field frequency is experimentally challenging.

1. Introduction

The photonic spin Hall effect (SHE) is a fundamental phenomenon in light–matter interactions, characterized by the transverse spatial separation of light based on its polarization states at an interface.[1] This effect arises from the spin–orbit interaction of light,[2] where the polarization of photons plays a role analogous to the electron spin in conventional electronic SHE.[1,3] Much like in electronic systems where a gradient in electric potential leads to spin separation, the photonic SHE results from refractive index gradients, substituting the electron's spin with the photon's polarization.[4,5] The theoretical basis for the photonic SHE was first proposed by Onoda et al. in 2004,[1] and was later extended through rigorous analysis by Bliokh.[3] In 2008, Hosten and Kwiat provided experimental validation of the effect using weak measurement techniques.[6]

The photonic SHE is now widely recognized as a consequence of the spin–orbit interaction of photons, consistent with the fundamental principle of angular momentum conservation in light.[7,8] To enhance the visibility and magnitude of this effect, several theoretical and experimental techniques have been developed. Among them, weak value amplification has proven particularly effective, enabling significant magnification of the transverse spin-dependent displacement characteristic of the photonic SHE.[9,10] This phenomenon has found applications in high-precision optical metrology, quantum information processing, and the design of advanced photonic devices for optical sensing and imaging.[11–13]

Another intriguing class of phenomena arises in Rydberg atoms–atoms in highly excited states where a single valence electron is promoted to a high-energy orbital, resulting in a large principal quantum number. Although any atomic species can, in principle, be excited to a Rydberg state, neutral alkali atoms are particularly favorable candidates. This is due to their single valence electron, which facilitates excitation to high-lying energy levels, making them especially suitable for experimental studies.[14]

Due to their single-electron excitation, Rydberg atoms exhibit long radiative lifetimes, high polarizability, and strong dipole–dipole or van der Waals (vdW) interactions, making them more advantageous than typical single atoms. These strong interactions can inhibit all but one optical excitation within a volume of several micrometers, a phenomenon known as the dipole blockade.[15,16] Within this volume, typically referred to as a blockade sphere, atoms exhibit collective behavior and can be modeled as an effective two-level system, commonly referred to as

M. Abbas, W. Liu, P. Zhang
Ministry of Education Key Laboratory for Nonequilibrium Synthesis and Modulation of Condensed Matter
Shaanxi Province Key Laboratory of Quantum Information and Quantum Optoelectronic Devices
School of Physics
Xi'an Jiaotong University
Xi'an 710049, China
E-mail: zhangpei@mail.ustc.edu.cn
H. R. Hamedi
Institute of Theoretical Physics and Astronomy
Vilnius University
Sauletekio 3, Vilnius 10257, Lithuania
E-mail: hamid.hamedi@tfai.vu.lt

The ORCID identification number(s) for the author(s) of this article can be found under https://doi.org/10.1002/andp.202500194

DOI: 10.1002/andp.202500194

a superatom (SA). This concept enables coherent manipulation and entanglement of collective excitations in cold Rydberg atomic ensembles.[15] Due to the strong Rydberg–Rydberg interactions, the excitation of one atom to a Rydberg state inhibits the excitation of nearby atoms within the same volume, thereby limiting the system to a single Rydberg excitation per blockade region. This dipole blockade mechanism makes Rydberg atoms promising candidates for applications in single-photon quantum devices.[17–20]

Recent theoretical developments have modeled Rydberg-dressed Electromagnetically Induced Transparency (EIT) systems using three-level atoms in a cascade configuration. These models employ mean-field approximations and two-photon correlations within a coarse-grained description of the medium composed of superatoms.[14] In Rydberg atomic systems, EIT exhibits nonlinear behavior due to strong interatomic interactions mediated by Rydberg excitations. The characteristics of the transparency window can be modulated by adjusting the intensity of the probe field. This theoretical approach has been generalized beyond the weak-probe regime to include higher-order nonlinear effects.[21] Moreover, experiments with ultracold Rydberg ensembles have revealed the presence of strongly interacting dark-state polaritons under EIT conditions, highlighting the intricate coupling between photons and collective atomic excitations in these media. More recently, the dynamics of a hybrid optomechanical system coupled to a Rydberg superatom have also been investigated, further expanding the potential of Rydberg-based quantum technologies.[22]

Motivated by previous investigations into light-matter interactions in strongly interacting atomic systems,[14] we explore the manifestation of photonic SHE in a Rydberg medium structured as a collection of SAs. Each SA consists of a group of three-level atoms arranged in a ladder-type configuration, where collective behavior arises due to pronounced dipole–dipole interactions and excitation blockade effects. Our study focuses on the role of spin–orbit coupling modulated by the dipole blockade effect in governing the transverse spin-dependent deflection of light in this highly tunable platform.

The photonic SHE has become a cornerstone in the study of spin-dependent light-matter interactions, with various atomic configurations offering valuable insights into this phenomenon.[23–27] While these conventional atomic systems have advanced our understanding, they remain constrained by limited tunability, weak nonlinearities, and reduced coherence at the few-photon level. In contrast, Rydberg atomic ensembles present a fundamentally superior platform for exploring the photonic SHE, owing to their exceptional and tunable electromagnetic properties. Rydberg atoms exhibit exaggerated characteristics, such as ultra-long radiative lifetimes, giant polarizabilities, and strong long-range dipole–dipole interactions. These features enable the realization of the dipole blockade effect, where collective excitation dynamics in mesoscopic ensembles (Rydberg superatoms) produce coherent quantum behavior at the single- or few-photon level. Such blockade-induced nonlinearity and collective coherence significantly enhance sensitivity to spin–orbit coupling effects, making the system highly responsive to probe field variations and external control parameters.

Consequently, using the non-linear and collective optical response of Rydberg superatoms, we aimed to uncover novel mechanisms for manipulating the photonic SHE. The insights gained may pave the way for advanced applications in precision metrology, dynamic optical switching, and quantum photonic information processing.

2. Proposed Model

2.1. The Photonic Spin Hall Effect

We investigate the interaction of a monochromatic Gaussian probe beam, containing both transverse-electric (TE) along with transverse-magnetic (TM) polarization components, as it impinges from vacuum onto the cavity mirror M_1 at an incidence angle θ_i, as depicted in **Figure** 1a. Upon interacting with the three-layer structure, the incident beam may either transmit through or reflect from the interfaces. In the reflection process, the left circularly polarized (LCP) components as well as right circularly polarized (RCP) experience transverse shifts in opposite directions along the y axis - perpendicular to the plane of incidence arising from the spin-orbit coupling of light. This spin-dependent spatial separation is termed the photonic SHE. For the multilayer configuration under consideration, the complex reflection coefficients for TM and TE polarizations, denoted by R_p and R_s respectively, are obtained through the transfer-matrix formalism and are given by:

$$R_{p,s} = \frac{\mathcal{R}^{12}_{p,s} + \mathcal{R}^{23}_{p,s}\exp(2ik_{2z}q)}{1 + \mathcal{R}^{12}_{p,s}\mathcal{R}^{23}_{p,s}\exp(2ik_{2z}q)} \tag{1}$$

here, q denotes the thickness of the intracavity medium, while $\mathcal{R}^{12}_{M,E}$ along with $\mathcal{R}^{23}_{M,E}$ represent the reflection coefficients at mirror–Rydberg atomic medium interface and the Rydberg medium–second mirror interface. For the overall two-interface system involving the top mirror, the intracavity medium, and the bottom mirror, the effective reflection coefficient for TM-polarized waves is expressed as:

$$\mathcal{R}^{ij}_{p} = \frac{\varepsilon_j k_{iz} - \varepsilon_i k_{jz}}{\varepsilon_j k_{iz} + \varepsilon_i k_{jz}} \tag{2}$$

and for TE polarized is

$$\mathcal{R}^{ij}_{s} = \frac{k_{iz} - k_{jz}}{k_{iz} + k_{jz}} \tag{3}$$

In this formulation, $k_{iz} = \sqrt{k_0^2\epsilon_i - k_x^2}$ denotes the component of the wave vector normal to the interfaces within the i-th layer, while $k_x = \sqrt{\epsilon_1}k_0\sin(\theta_i)$ characterizes the wave vector component parallel to the x-axis. Here, $k_0 = 2\pi/\lambda$ is the magnitude of the wave number in vacuum, with λ being the wavelength of the incident light. As evident from Equation (1), the reflection behavior is intrinsically linked to the dielectric response ϵ_2 of the nonlinear Rydberg atomic medium, which can be dynamically tuned by adjusting the susceptibility χ^{NL}. This tunability enables precise control over the photonic SHE of the reflected beam. In the reflection configuration, considering a TM-polarized Gaussian probe beam, the amplitudes of the RCP along with LCP

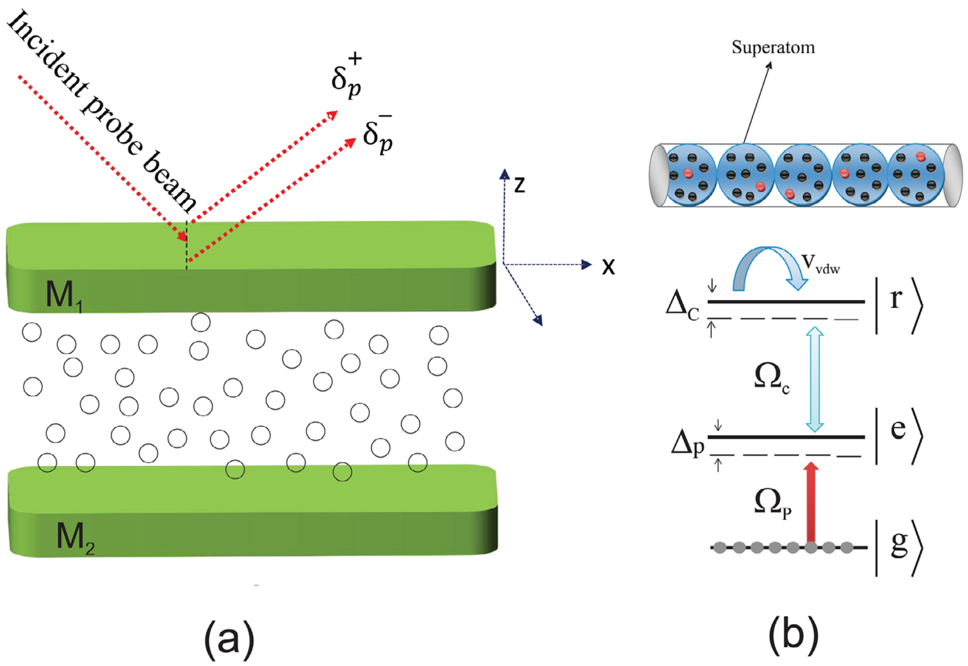

Figure 1. a) A schematic representation of a three-layer cavity system, featuring two mirrors, M_1 and M_2, with Rydberg atoms coherently positioned between the dielectric layers. b) A diagram illustrating the configuration of superatoms along with their corresponding energy levels in a three-level cascade atomic system.

components of the reflected field are organized as follows:[28]

$$\mathcal{E}_r^{\pm}(x_r, y_r, z_r) = \frac{\omega_0}{\omega} \exp\left[-\frac{x_r^2 + y_r^2}{\omega}\right] \times \left[R_p - \frac{2ix_r}{k\omega}\frac{\partial R_p}{\partial \theta} \mp \frac{2y_r \cot[\theta]}{k\omega}(R_s + R_p)\right] \tag{4}$$

here, $\omega = \omega_0 \left[1 + \left(\frac{2z_r}{k_1\omega_0^2}\right)^2\right]^{1/2}$ describes the beam radius as a function of propagation, where $z_r = \frac{k_1\omega_0^2}{2}$ denotes the Rayleigh range, and ω_0 specifies the waist radius of the incident Gaussian beam. The coordinates (x_r, y_r, z_r) define the reference frame associated with the reflected beam, while the superscript ± distinguishes between the two spin (polarization) states. Based on this framework, the transverse shift of the reflected beam can be determined as:[29,30]

$$\delta_p^{\pm} = \frac{\int y|\mathcal{E}_r^{\pm}(x_r, y_r, z_r)|^2 dx_r dy_r}{\int |\mathcal{E}_r^{\pm}(x_r, y_r, z_r)|^2 dx_r dy_r} \tag{5}$$

The expressions for the transverse spin shifts δ_p^+ as well as δ_p^- in a cavity-integrated three-level Rydberg atomic system can be formulated as follows:[30,31]

$$\delta_p^{\pm} = \mp \frac{k_1\omega_0^2 \mathrm{Re}[1 + \frac{R_s}{R_p}]\cot\theta_i}{k_1^2\omega_0^2 + |\frac{\partial ln R_p}{\partial \theta_i}|^2 + |(1 + \frac{R_s}{R_p})\cot\theta_i|^2} \tag{6}$$

Here, $\delta_p^{\pm}$ represents the transverse displacement corresponding to the LCP as well as RCP components of the incident beam, with $k_1 = \sqrt{\epsilon_1}k$ being the wave vector inside the initial medium. In the subsequent analysis, our attention will primarily be directed toward the transverse shift δ_p^+ associated with the LCP. Given that the displacements for the two spin states possess equal magnitudes but opposite signs, adjusting one simultaneously influences the other.

The inclusion of a nonlinear Rydberg atomic medium within the cavity substantially influences the photonic SHE of the reflected probe beam. The key factor is the tunable dielectric permittivity ε_2, which depends on the nonlinear susceptibility χ^{NL} of the Rydberg ensemble. This susceptibility is highly sensitive to the Rydberg blockade, probe as well as control field intensities, and detunings. As a result, the reflection coefficients R_s and R_p are no longer static but become dynamically controllable, leading to enhanced modulation of the transverse spin-dependent shift $\delta_p^{\pm}$. This tunability stands in contrast to conventional linear media and offers a powerful platform for exploring and engineering spin-dependent optical effects using strongly interacting atomic systems.

2.2. Modeling the Optical Response of Rydberg Atoms

We consider a system that contains several Rydberg superatoms, denoted by n_{SA}, where each superatom consists of a cold atomic ensemble confined within a volume V and simultaneously driven by two optical fields that control their behavior. In this configuration, the strong dipole–dipole interactions characteristic of Rydberg atoms lead to a phenomenon known as the dipole blockade. This effect ensures that within each superatom, only a single atom can be excited to the Rydberg state at any given time, effectively suppressing further excitations. As a result, the atoms within each superatom exhibit collective quantum behavior, functioning as a unified system that shares the excitation coherently.

As illustrated in Figure 1a, a weak probe beam and a strong control field coherently interact with the atomic ensemble. Each SA comprises a dense cloud of ultracold ^{87}Rb atoms, featuring a three-level cascade configuration with quantum states defined as $|\mathrm{g}\rangle \equiv 5S_{1/2}|F=2, m_F=2\rangle$, $|\mathrm{e}\rangle \equiv 5P_{3/2}|F=3, m_F=3\rangle$, and $|\mathrm{r}\rangle \equiv 60S_{1/2}$. Atoms collectively pair with optical fields in a ladder-type interaction scheme, as depicted in Figure 1b.

Within a ladder-type three-level atomic configuration, the probe field with Rabi frequency Ω_p excites atoms from the ground state $|\mathrm{g}\rangle$ to an intermediate state $|\mathrm{e}\rangle$. Simultaneously, a control field characterized by Rabi frequency Ω_c drives the transition from the intermediate level $|\mathrm{e}\rangle$ to a highly excited Rydberg state $|\mathrm{r}\rangle$. The interaction between Rydberg atoms is described by a vdW potential, given by $\Delta(r_i - r_j) = \frac{C_6}{|r_i - r_j|^6}$,[14] where r_i and r_j denote the spatial coordinates of the interacting atomic pair.

The total Hamiltonian governing the dynamics of the atomic ensemble interacting with classical optical fields and interatomic van der Waals interactions is expressed as:

$$H = H_{\mathrm{atom}} + H_{\mathrm{int}} + H_{\mathrm{vdW}} \tag{7}$$

where the respective terms are defined as follows:

$$\begin{aligned} H_{\mathrm{atom}} &= -\hbar \sum_{j=1}^{N} \left[\Delta_p \sigma_{ee}^{(j)} + \Delta_2 \sigma_{rr}^{(j)} \right] \\ H_{\mathrm{int}} &= -\hbar \sum_{j=1}^{N} \left[\Omega_p \sigma_{eg}^{(j)} + \Omega_c \sigma_{re}^{(j)} + \mathrm{H.c.} \right] \\ H_{\mathrm{vdW}} &= \hbar \sum_{i<j}^{N} \sigma_{rr}^{(i)} \Delta(r_i - r_j) \sigma_{rr}^{(j)} \end{aligned} \tag{8}$$

with detunings defined as $\Delta_p = \omega_p - \omega_{eg}$, $\Delta_c = \omega_c - \omega_{re}$, and $\Delta_2 = \Delta_p + \Delta_c$. Here, $\sigma_{\mu\nu}^{(j)}$ denotes the transition operator for the jth atom between states $|\mu\rangle$ and $|\nu\rangle$. In this formulation, the operator $\sigma_{\alpha\beta}^{(j)} = |\alpha\rangle_j\langle\beta|$ represents the transition between the states $|\alpha\rangle$ and $|\beta\rangle$ for the jth atom located at position r_j.

By solving the equations derived from Equations (7) and (8), we obtain the following set of Heisenberg-Langevin equations governing the atomic dynamics:

$$\begin{aligned} \dot{\sigma}_{gg}^{(j)} &= i\Omega_p^* \sigma_{ge}^{(j)} - i\Omega_p \sigma_{eg}^{(j)} + \Gamma_e \sigma_{ee}^{(j)}, \\ \dot{\sigma}_{ee}^{(j)} &= i\Omega_p \sigma_{eg}^{(j)} - i\Omega_p^* \sigma_{ge}^{(j)} - i\Omega_c \sigma_{re}^{(j)} - i\Omega_c^* \sigma_{er}^{(j)} + \Gamma_r \sigma_{rr}^{(j)} + \Gamma_e \sigma_{ee}^{(j)}, \\ \dot{\sigma}_{ge}^{(j)} &= \left(i\Delta_p - \gamma_{ge}\right)\sigma_{ge}^{(j)} + i\Omega_p \left(\sigma_{gg}^{(j)} - \sigma_{ee}^{(j)}\right) + i\Omega_c^* \sigma_{gr}^{(j)} \\ \dot{\sigma}_{gr}^{(j)} &= \left[i\left(\Delta_2 - S(r)\right) - \gamma_{gr}\right]\sigma_{gr}^{(j)} + i\Omega_c \sigma_{ge}^{(j)} - i\Omega_p \sigma_{er}^{(j)} \\ \dot{\sigma}_{er}^{(j)} &= \left[i\left(\Delta_p - S(r)\right) - \gamma_{er}\right]\sigma_{er}^{(j)} - i\Omega_p^* \sigma_{gr}^{(j)} + i\Omega_c \left(\sigma_{ee}^{(j)} - \sigma_{rr}^{(j)}\right), \end{aligned} \tag{9}$$

where Γ_e and Γ_r are the spontaneous decay rates of the excited and Rydberg states, respectively, and $S(r)$ accounts for the spatially dependent van der Waals interaction shift. In this context, Γ_e denotes the spontaneous decay rate of the excited state, while γ_{ge}, γ_{er}, and γ_{gr} represent the corresponding dephasing rates for the atomic transitions. Due to the inherently longer lifetime of the Rydberg state, it follows that $\gamma_{ge} \gg \gamma_{gr}$. The quantity $S(r)$ accounts for the energy shift arising from the van der Waals (vdW) interaction experienced by an atom in the Rydberg state $|r\rangle$ at position r, and it is given by

$$S(r) = \sum_{i<j}^{n_{\mathrm{SA}}} \Delta(r - r_j)\sigma_{rr} \tag{10}$$

here $\Delta(r - r_j)$ characterizes the vdW interaction potential between atoms located at r and r_j, and σ_{rr} corresponds to the population operator associated with the Rydberg state.

By considering the system in steady state, the solution to Equation (9) takes the form:

$$\begin{aligned} \sigma_{ge} &= \frac{i\Omega_p\left[\gamma_{gr} - i(-S + \Delta_2)\right]}{\left(\gamma_{ge} - i\Delta_p\right)\left[\gamma_{gr} - i(-S + \Delta_2)\right] + \Omega_c^2} \\ \sigma_{gr} &= -\frac{\Omega_c\Omega_p}{\left(-i\Delta_p + \gamma_{ge}\right)\left[\gamma_{gr} - i(-S + \Delta_2)\right] + \Omega_c^2} \end{aligned} \tag{11}$$

Following the method outlined in Ref. [14] and considering the steady-state solution of Equation (9) in the absence of the vdW shift $S(r)$, we express σ_{rr} as:

$$\langle \sigma_{rr} \rangle = \sigma_{rg}\sigma_{gr} \tag{12}$$

Assuming the condition $\gamma_{gr} \ll \gamma_{ge}$ and $\Delta_p < \gamma_{ge}$, we obtain the following approximation for σ_{rr}:

$$\langle \sigma_{rr} \rangle \approx \frac{|\Omega_c|^2 |\Omega_p|^2}{|\Omega_c|^4 + \Delta_2^2 \gamma_{ge}^2} \tag{13}$$

We now analyze the vdW-induced energy shift occurring in a medium composed of an ensemble of SAs. To incorporate this effect, we replace the single-atom population term σ_{rr} with Σ_{rr}, which denotes the collective population of atoms excited to the Rydberg state across all SAs. The presence of a Rydberg-excited atom induces a distance-dependent energy shift $\Delta(R)$ on neighboring atoms via vdW interactions. This shift inhibits further Rydberg excitations within a characteristic interaction volume V_{SA}, a phenomenon known as the Rydberg blockade.[15]

The number of atoms residing in each SA is given by $n_{SA} = \rho(r)V_{SA}$, where $\rho(r)$ is the local atomic density. Under blockade conditions, each SA is effectively restricted to a single Rydberg excitation within V_{SA}. As a result, the entire medium can be described as a spatial array of such SAs, with the total number contained in a volume V expressed as $N_{SA} = \rho_{SA}V$, where ρ_{SA} is the SA density. The overall van der Waals shift at a specific position r is then given by:

$$S(r) = \sum_{j}^{N_{SA}} \Delta(r - r_j)\Sigma_{RR}(r_j) = \bar{\Delta}\Sigma_{RR}(r) + s(r) \tag{14}$$

In Equation (14), the first term on the right-hand side accounts for the contribution from the excited SA located at $r_j = r$, where

$\Sigma_{RR}(r) \to 1$. This results in a divergent vdW shift within the SA, since the average shift $\bar{\Delta}(0) \approx \frac{1}{V_{SA}} \int_{V_{SA}} \Delta(r')\, d^3 r' \to \infty$.

The second term, $s(r)$, represents the vdW shift arising from other SAs located outside the local volume. It is defined as:

$$s(r) = \sum_{j \neq j_r}^{N_{SA}} \Delta(r - r_j)\Sigma_{RR}(r_j) \tag{15}$$

To evaluate $s(r)$, we employ a mean-field approximation following the method in Ref. [32]. By replacing the discrete sum with a continuous spatial average, we obtain:

$$\langle s(r) \rangle = \frac{w}{8} \langle \Sigma_{RR}(r) \rangle \tag{16}$$

where $w = \frac{|\Omega_c|^2}{\gamma_e}$ denotes the half-width of the Lorentzian profile characterizing the Rydberg population distribution.

We emphasize that this mean-field approach replaces the sum over distant SAs with an integral over space, assuming a dilute and homogeneous SA distribution. Under these conditions, inter-SA correlations are negligible, and the vdW shift from external SAs can be reliably approximated by a spatial average. As detailed in Ref. [32], this method accurately captures the long-range interaction-induced shift $s(r)$, provided that excitation dynamics are slow compared to inter-SA separation and collective blockade effects dominate. The simulation parameters used here satisfy these conditions, validating the use of the mean-field model for describing the nonlinear optical response arising from vdW interactions.

The analytical form of $s(r)$ can be derived by computing $\Sigma_{RR}(r)$, which accounts for the total Rydberg excitation within a SA. As each SA consists of multiple atoms confined within a blockade region, its internal dynamics can be efficiently described using collective states and operators. The corresponding ground and singly excited collective Rydberg states are represented as:

$$|G\rangle = |g_1, g_2, g_3, \dots, g_{n_{SA}}\rangle \tag{17}$$

and

$$|R^{(1)}\rangle = \frac{1}{\sqrt{n_{SA}}} \sum_{j}^{n_{SA}} |g_1, g_2, g_3, \dots, r_j, \dots, g_{n_{SA}}\rangle \tag{18}$$

For the SA in the ground state $|G\rangle$, $\Sigma_{RR}(r)$ can be written as:[32]

$$\Sigma_{RR} = \Sigma_{RG} \cdot \Sigma_{GR} \tag{19}$$

which replaces Equation (12), where:

$$\Sigma_{GR} = \frac{\sqrt{n_{SA}}\Omega_c \Omega_p \Sigma_{GG}}{\Delta_2(i\gamma_{eg} + \Delta_p) - |\Omega_c|^2} \tag{20}$$

Using Equations (19), (20), and the condition $\Sigma_{GG} + \Sigma_{RR} = 1$, the final expression for Σ_{RR} is:

$$\Sigma_{RR} = \frac{n_{SA}|\Omega_p|^2|\Omega_c|^2}{|\Omega_p|^2|\Omega_c|^2 n_{SA} + \left[-|\Omega_c|^2 + \Delta_2\Delta_p\right]^2 + \gamma_{eg}^2\Delta_2^2} \tag{21}$$

Equations (14) through Equation (21) collectively highlight how the Rydberg blockade mechanism induces nonlinearity in the atomic medium. This nonlinearity stems from the vdW interaction-induced shift, which directly influences the collective Rydberg population Σ_{RR}. The value of Σ_{RR} depends on both the probe field Rabi frequency Ω_p and the number of atoms per superatom n_{SA}. In the absence of the vdW-induced shift (i.e., when $s(r) = 0$), the optical response of the medium becomes nearly independent of probe field intensity.

The nonlinear susceptibility χ^{NL}, incorporating the impact of dipole blockade and long-range interactions, is given by:

$$\chi^{NL} = \beta \Bigg[\Sigma_{RR} \frac{i\gamma_{eg}}{\gamma_{eg} - i\Delta_p} + (1 - \Sigma_{RR}) \times \frac{i\gamma_{eg}}{\gamma_{eg} - i\Delta_p + |\Omega_c|^2\left[\gamma_{rg} - i(\Delta_2 - \langle s(r)\rangle)\right]^{-1}} \Bigg] \tag{22}$$

where $\beta = \frac{\mathcal{N}|\mu_{eg}|^2}{4\pi\hbar\epsilon_0}$ is the coupling constant that links atomic density and dipole strength to the optical response.

From Equation (21), it is evident that Σ_{RR} increases with both Ω_p and n_{SA}, reflecting stronger collective coupling. In the limit $\Sigma_{RR} \to 1$, corresponding to strong blockade, the medium behaves effectively as a saturated two-level absorber with suppressed EIT transparency. Conversely, when $\Sigma_{RR} \to 0$, the system reverts to a standard three-level EIT configuration with low nonlinearity. Therefore, the nonlinear susceptibility χ^{NL} is strongly modulated by the blockade-induced population saturation. The parameter n_{SA} plays a central role: increasing it enhances blockade strength and nonlinear absorption, while reducing it preserves transparency. As such, n_{SA} serves as a key control knob for engineering tunable nonlinearity in cold Rydberg ensembles. This tunability is crucial for applications in photon switching, nonclassical light generation, and quantum information processing.

3. Numerical Insights and Discussion

In this section, we present the results of our numerical simulations, using parameter values aligned with those reported in experimental studies.[33] The chosen parameters are $\gamma = 1$ MHz, $\Omega_c = 5\gamma$, $n_{SA} = 20$, $\Delta_p = \Delta_c \approx 0$, $\gamma_{eg} = 3\gamma$, and $\gamma_{rg} = 0.01\gamma$, $\mathcal{N} = 10^{12}\ \mathrm{cm}^{-3}$, $\boldsymbol{\mu}_{eg} = 1.269 \times 10^{-29}$ Cm. To explore the polarization-dependent photonic SHE, we set the dielectric permittivities as $\epsilon_0 = 1$, $\epsilon_1 = 2.22$, $\epsilon_2 = 1 + \chi^{NL}$, and $\epsilon_3 = 2.22$, $\lambda = 780$nm, with the cavity thickness $q = 0.5\ \mu$m.

Figure 2 presents the behavior of both the absorptive and dispersive parts of the susceptibility, obtained from Equation (22), as functions of the probe detuning Δ_p. The system's optical response exhibit a strong dependence on the probe Rabi frequency Ω_p. To highlight this influence, two specific values are considered: a) $\Omega_p = 0.5\gamma$ and b) $\Omega_p = 0.005\gamma$. For the case of the strongest probe field, shown in Figure 2a, the system exhibits significant absorption and associated normal dispersion. In this regime, the higher intensity of the probe field enhances excitation into the Rydberg state, thereby strengthening dipole–dipole interactions. This behavior can be attributed to the strong

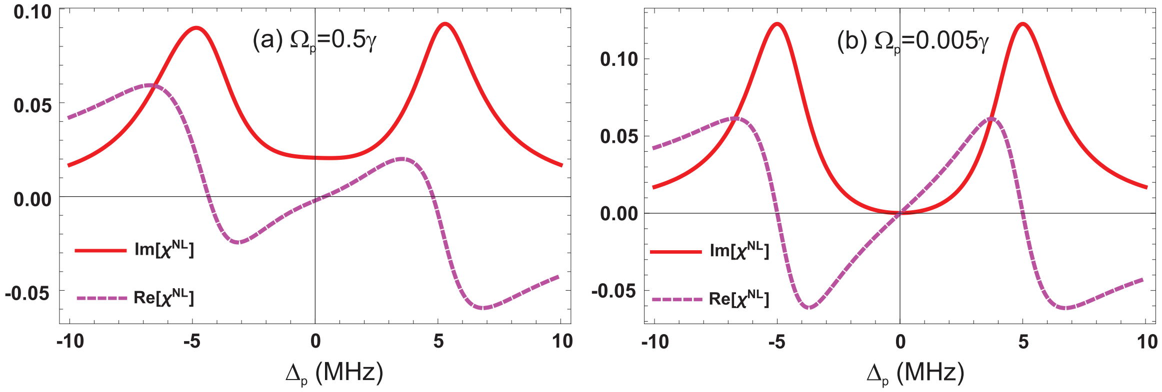

Figure 2. Absorption spectrum (depicted by the red solid line) and dispersion spectrum (shown by the pink dashed line) as a function of probe field strength at two different values: a) $\Omega_p = 0.5\gamma$ and b) $\Omega_p = 0.005\gamma$. The remaining parameters are: $\mathcal{N} = 10^{12}$ cm^{-3}, $\boldsymbol{\mu}_{eg} = 1.269 \times 10^{-29}$ Cm, $\gamma = 1$ MHz, $\Omega_c = 5\gamma$, $n_{SA} = 20$, $\Delta_c = 0$, $\gamma_{eg} = 3\gamma$, and $\gamma_{rg} = 0.01\gamma$.

Rydberg blockade effect that emerges at higher probe field intensities, where $\Sigma_{RR} \to 1$. Under this regime, the medium effectively behaves as a two-level absorbing system, since the excitation of additional Rydberg atoms within a blockade volume is suppressed. Consequently, the probe field can induce transitions in only one atom per SA, while excess photons interact with the remaining two-level atoms, leading to enhanced absorption. This mechanism accounts for the pronounced absorption observed in Figure 2a.

In contrast, for a weaker probe field ($\Omega_p = 0.005\gamma$), a transparency window emerges along with a steeper slope of normal dispersion compared to the previous case, as illustrated in Figure 2b. In this regime, EIT becomes dominant. The coherence established between the atomic states significantly suppresses absorption, enabling the probe field to propagate through the medium with minimal loss. These results are in good agreement with the findings reported in Ref. [14], further supporting the accuracy of our theoretical model and numerical simulations.

The probe field Rabi frequency Ω_p hence plays a crucial role in shaping the absorption and dispersion characteristics of the medium, thereby influencing its permittivity ϵ_2. This sensitivity in permittivity directly impacts the reflection coefficients and the photonic SHE. To investigate these effects, we examine $|R_s|$ and $|R_p|$ as functions of the incident angle θ_i, with results presented in **Figure 3**. Two cases are considered: a) $\Omega_p = 0.5\gamma$ and b) $\Omega_p = 0.005\gamma$.

For $\Omega_p = 0.5\gamma$, at approximately $\theta_i \approx 25°$, $|R_p|$ vanishes, while $|R_s|$ remains slightly nonzero, as illustrated in Figure 3a. This nonzero reflection arises from residual birefringence caused by permittivity alterations at higher probe field intensities. As the angle increases, $|R_p|$ remains negligible, whereas $|R_s|$ shows a pronounced increase near the Brewster angle ($\theta_i \approx 33.8237°$).

In the case of $\Omega_p = 0.005\gamma$, at around $\theta_i \approx 25°$, both $|R_p|$ and $|R_s|$ become exactly zero, as shown in Figure 3b. This indicates that at lower probe field intensities, the system reaches a condition where no reflection occurs for either polarization. However, beyond this point, $|R_s|$ begins to rise significantly near $\theta_i \approx 33.8237°$, mirroring the behavior observed for $\Omega_p = 0.5\gamma$. Thus, at the Brewster angle, $|R_p|$ is completely suppressed, while $|R_s|$ exhibits a sharp increase, consistent with Figure 3a.

Next, in **Figure 4a**, we present the ratio $|R_s|/|R_p|$ for $\Omega_p = 0.5\gamma$. Owing to strong absorption under a high probe field Rabi

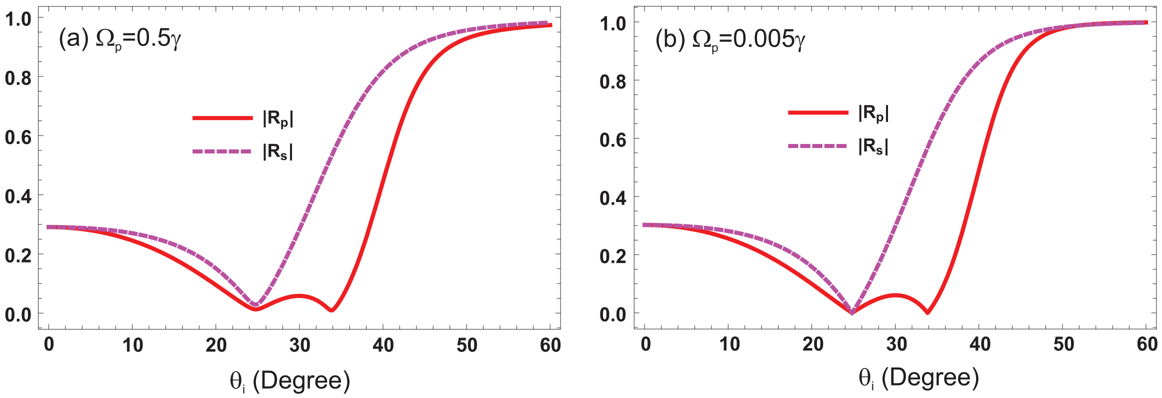

Figure 3. Variation of the coefficients $|R_p|$ and $|R_s|$ respectively, with respect to the incidence angle θ_i, is depicted for two probe Rabi frequencies: a) $\Omega_p = 0.5\gamma$ and b) $\Omega_p = 0.005\gamma$. The simulations are conducted under identical conditions: atomic number density $\mathcal{N} = 10^{12}$ cm^{-3}, dipole transition moment $\boldsymbol{\mu}_{eg} = 1.269 \times 10^{-29}$ Cm, spontaneous emission rate $\gamma = 1$ MHz, control field strength $\Omega_c = 5\gamma$, number of superatoms $n_{SA} = 20$, near-resonant driving with $\Delta_p = \Delta_c \approx 0$, decoherence parameters $\gamma_{eg} = 3\gamma$ and $\gamma_{rg} = 0.01\gamma$, permittivities $\epsilon_1 = \epsilon_3 = 2.22$, probe wavelength $\lambda = 780$ nm, and thickness of the intracavity medium $q = 0.5$ µm.

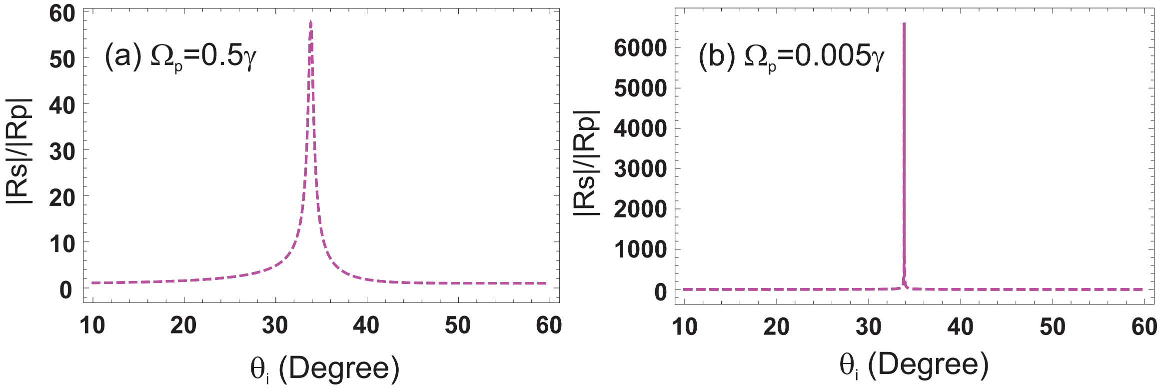

Figure 4. The dependence of the ratio $\left|R_s/R_p\right|$, on the incidence angle θ_i is illustrated for two distinct probe field strengths: a) $\Omega_p = 0.5\gamma$, and b) $\Omega_p = 0.005\gamma$. These results are obtained under the following fixed conditions: atomic number density $\mathcal{N} = 10^{12}$ cm^{-3}, dipole matrix element $\boldsymbol{\mu}_{eg} = 1.269 \times 10^{-29}$ Cm, natural linewidth $\gamma = 1$ MHz, control Rabi frequency $\Omega_c = 5\gamma$, ensemble size of $n_{SA} = 20$ superatoms, vanishing probe and control detunings ($\Delta_p = \Delta_c \approx 0$), decoherence rates $\gamma_{eg} = 3\gamma$ and $\gamma_{rg} = 0.01\gamma$, background dielectric constants $\epsilon_1 = \epsilon_3 = 2.22$, probe wavelength $\lambda = 780$ nm, and thickness of the intracavity medium $q = 0.5$ µm.

frequency, the ratio remains relatively modest, with a value around 60. In contrast, Figure 4b reveals a pronounced enhancement at the incident angle $\theta_i \approx 33.8237°$, where the ratio sharply increases to a maximum of approximately 6800—indicative of a resonance peak condition. As indicated by Equation (6), a higher ratio of $|R_s|/|R_p|$ contributes to an enhanced photonic SHE. The sharp enhancement in the ratio $|R_s|/|R_p|$ around the incident angle $\theta_i \approx 33.8237°$ is primarily attributed to the diminished Rydberg blockade effect at lower probe field intensities. This reduction permits nonlinear absorption to become more pronounced by limiting multiple excitations, thereby yielding a substantial contrast between $|R_s|$ and $|R_p|$.

We now examine the transverse spin-dependent displacement resulting from the photonic SHE, with particular attention to the LCP component, denoted as δ_p^+. **Figure 5** illustrates the variation of δ_p^+ as a function of the incidence angle θ_i for two different probe field strengths: a) $\Omega_p = 0.5\gamma$ and b) $\Omega_p = 0.005\gamma$.

At high probe intensity, as shown in Figure 5a, the displacement remains relatively small throughout the angular domain. This behavior is attributed to enhanced Rydberg excitation and dipole–dipole interactions, which lead to significant absorption and broad dispersion, thereby reducing spin-dependent light–matter coupling. In contrast, under weak probe conditions (Figure 5), the system operates in the EIT regime with low absorption and steep dispersion. This enhances spin–orbit interactions, resulting in a noticeable increase in δ_p^+.

In both scenarios, the transverse shift exhibits a sign change near the Brewster angle ($\theta_i \approx 33.8237°$), transitioning from positive to negative. This phenomenon originates from a π-phase difference between the Fresnel reflection coefficients R_s and R_p, influencing polarization-sensitive reflection.

As shown in Figure 5, the probe Rabi frequency Ω_p plays an important role in tuning the optical response of the Rydberg atomic system. In Figure 5a, higher Ω_p leads to stronger excitation and

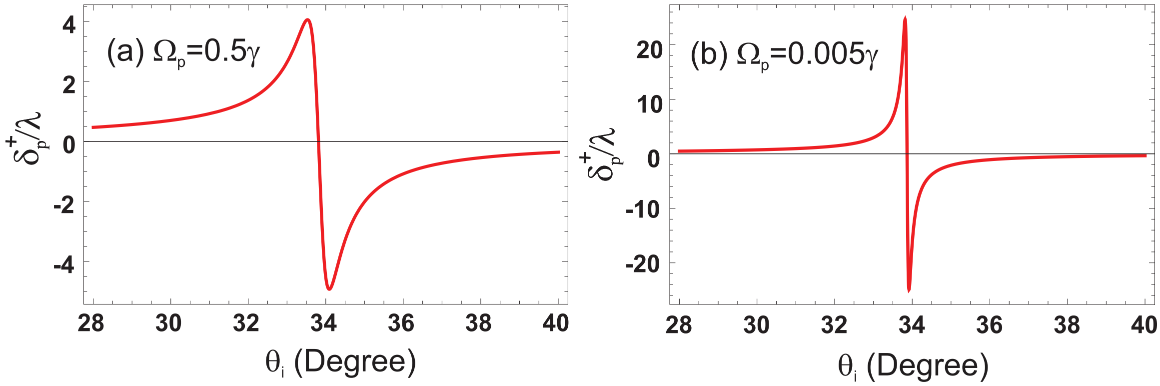

Figure 5. The variation of the photonic SHE, characterized by the displacement δ_p^+, is depicted as a function of the incident angle θ_i for two different values of the probe Rabi frequency: a) $\Omega_p = 0.5\gamma$ and b) $\Omega_p = 0.005\gamma$. The simulations are carried out with the parameters fixed as follows: atomic density $\mathcal{N} = 10^{12}$ cm^{-3}, transition dipole moment $\boldsymbol{\mu}_{eg} = 1.269 \times 10^{-29}$ Cm, spontaneous decay rate $\gamma = 1$ MHz, control field strength $\Omega_c = 5\gamma$, number of superatoms $n_{SA} = 20$, with detunings $\Delta_p = \Delta_c \approx 0$, decoherence rates $\gamma_{eg} = 3\gamma$ and $\gamma_{rg} = 0.01\gamma$, dielectric constants $\epsilon_1 = \epsilon_3 = 2.22$, operating wavelength $\lambda = 780$ nm, thickness of the intracavity medium $q = 0.5$ µm, and beam waist $\omega_0 = 50\ \lambda$.

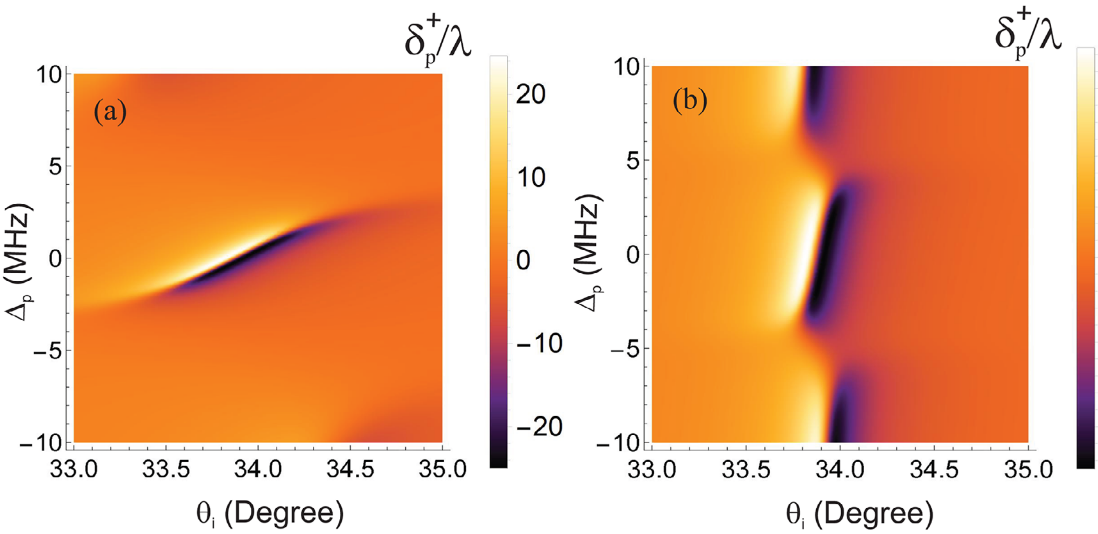

Figure 6. Density plot of the photonic SHE as influenced by the probe field detuning Δ_p and the angle of incidence θ_i. a) corresponds to an atomic ensemble with a number density of $\mathcal{N} = 10^{12}$ cm^{-3}, whereas b) illustrates the same for a reduced density of $\mathcal{N} = 10^{11}$ cm^{-3}, effectively a tenfold decrease. For both scenarios, the system parameters are fixed as follows: probe Rabi frequency $\Omega_p = 0.005\gamma$, natural linewidth $\gamma = 1$ MHz, control Rabi frequency $\Omega_c = 5\gamma$, number of superatoms $n_{SA} = 20$, control detuning $\Delta_c = 0$, decay rates $\gamma_{eg} = 3\gamma$ and $\gamma_{rg} = 0.01\gamma$, dielectric constants $\epsilon_1 = \epsilon_3 = 2.22$, transition wavelength $\lambda = 780$ nm, thickness of the intracavity medium $q = 0.5$ µm, electric dipole moment $\boldsymbol{\mu}_{eg} = 1.269 \times 10^{-29}$ Cm, and beam waist $\omega_0 = 50\,\lambda$.

interaction effects, which suppress the photonic SHE due to increased losses. Conversely, Figure 5b demonstrates that lower Ω_p preserves atomic coherence and promotes sharper dispersion, thereby amplifying the SHE. Hence, by varying Ω_p, one can dynamically modulate spin-dependent beam shifts through its impact on the medium's nonlinear susceptibility.

In **Figure 6**, the density distribution of the photonic SHE is shown as a function of the probe field detuning Δ_p and the angle of incidence θ_i, for two different atomic number densities: a) $\mathcal{N} = 10^{12}$ cm^{-3}, and b) $\mathcal{N} = 10^{11}$ cm^{-3}, corresponding to a tenfold decrease. All other parameters are identical to those used in Figure 5b.

At the higher atomic density of $\mathcal{N} = 10^{12}$ cm^{-3}, strong dipole-dipole interactions among Rydberg atoms give rise to a pronounced Rydberg blockade effect. This effect inhibits multiple excitations within a blockade volume, resulting in the formation of Rydberg superatoms—collective excitations that behave as single quantum entities. As a result, the photonic SHE becomes highly sensitive to the probe detuning Δ_p, particularly around $\Delta_p = 0$, where enhanced nonlinearities induce a marked shift in the photonic SHE response.

Conversely, at the reduced atomic density of $\mathcal{N} = 10^{11}$ cm^{-3}, the weakening of dipole-dipole interactions suppresses the Rydberg blockade, shifting the system from a regime of collective excitations to one characterized by independent atomic responses. This transition results in a diminished sensitivity of the photonic SHE to detuning, as indicated by a more uniform response across $\Delta_p = 0$ and $\Delta_p = \pm 10\gamma$.

From the perspective of spin-orbit interactions, variations in atomic density effectively modulate the coupling strength within the system. In high-density media, enhanced dipole-induced phase shifts influence polarization-dependent reflectivity, thereby amplifying the photonic SHE. In contrast, at lower densities, the phase evolution becomes more uniform, diminishing detuning-dependent spin-orbit effects and reducing the sensitivity of the SHE to variations in Δ_p.

Figure 7 presents the density plot of the photonic SHE as a function of the probe field Rabi frequency Ω_p and the angle of incidence θ_i, for two atomic number densities: a) $\mathcal{N} = 10^{12}$ cm^{-3}, and b) $\mathcal{N} = 10^{11}$ cm^{-3}. The probe detuning is fixed at $\Delta_p = 0$, with all other parameters matching those used in Figure 6.

In Figure 7a, at the higher atomic density of $\mathcal{N} = 10^{12}$ cm^{-3}, a pronounced enhancement of the photonic SHE is observed near the Brewster angle for specific values of Ω_p. The Brewster angle corresponds to the incidence angle at which p-polarized light is fully transmitted, eliminating reflection and significantly modifying the polarization state of the reflected field. At low Ω_p, spin-orbit interaction effects are more prominent, leading to an intensified photonic SHE in the vicinity of this angle.

In contrast, Figure 7b shows that at the lower atomic density of $\mathcal{N} = 10^{11}$ cm^{-3}, the photonic SHE becomes more pronounced and extends over a wider range of Ω_p values near the Brewster angle. This behavior can be attributed to the weakened interatomic interactions and reduced medium-induced perturbations, which allow spin-orbit coupling effects to persist even at higher probe field strengths.

Importantly, at lower atomic densities, the photonic SHE exhibits minimal sensitivity to variations in the probe Rabi frequency Ω_p, indicating a robust and nearly invariant response. This suggests that in low-density regimes, spin-orbit interactions remain effective with minimal influence from external driving fields, thereby enabling stable and consistent spin-dependent light manipulation.

The robustness of the photonic SHE near the Brewster angle presents promising prospects for photonic device applications. The ability to maintain a stable and enhanced photonic

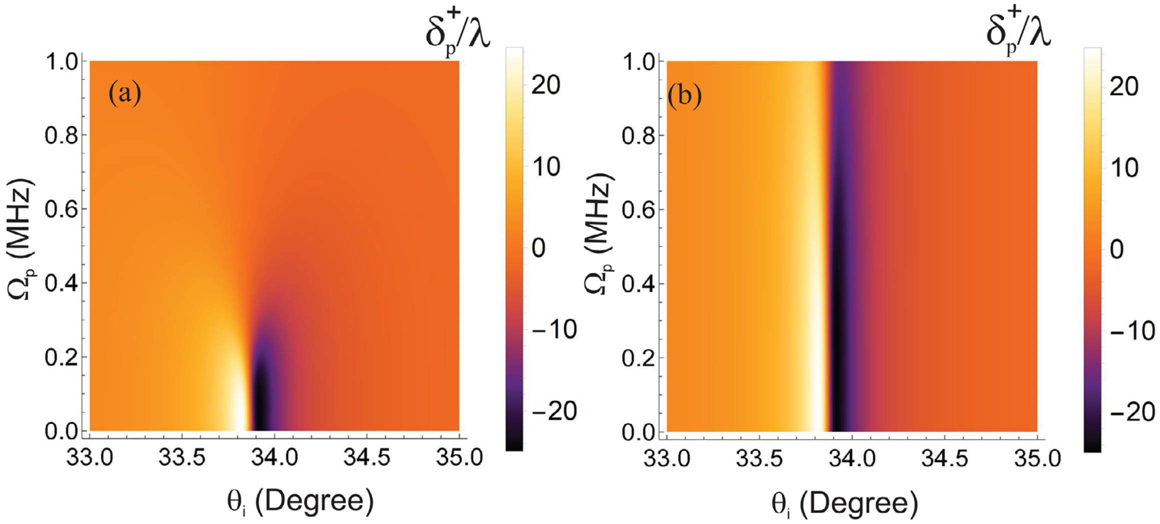

Figure 7. Photonic SHE density distribution as a function of the probe field Rabi frequency Ω_p and the angle of incidence θ_i. Panel (a) corresponds to an atomic ensemble characterized by a number density of $\mathcal{N} = 10^{12}$ cm^{-3}, while panel (b) depicts the effect of a reduced atomic density, $\mathcal{N} = 10^{11}$ cm^{-3}, representing a tenfold decrease. All other physical parameters are held constant: natural decay rate $\gamma = 1$ MHz, control field strength $\Omega_c = 5\gamma$, number of superatoms $n_{SA} = 20$, probe and control detunings $\Delta_p = \Delta_c \approx 0$, decay rates $\gamma_{eg} = 3\gamma$ and $\gamma_{rg} = 0.01\gamma$, dielectric permittivities $\epsilon_1 = \epsilon_3 = 2.22$, wavelength $\lambda = 780$ nm, thickness of the intracavity medium $q = 0.5$ µm, and the Gaussian beam waist $\omega_0 = 50\ \lambda$.

SHE under these conditions, regardless of probe intensity, could lead to the development of reliable optical sensors and advanced polarization-controlled switching systems.

These findings suggest that, at reduced atomic number density, the photonic SHE becomes considerably less sensitive to variations in both the probe field detuning and the Rabi frequency. Specifically, when the probe Rabi frequency is fixed at $\Omega_p = 0.005$ MHz, the photonic SHE exhibits an almost uniform response over a broad range of detuning values Δ_p, indicating detuning-independent behavior. Conversely, when $\Delta_p = 0$, the photonic SHE shows minimal variation with respect to Ω_p, highlighting its resilience to changes in probe field intensity. These observations emphasize the crucial role of atomic density in modulating the spin-dependent optical response in Rydberg atomic systems. This robustness against variations in both detuning and probe intensity points to the potential of low-density atomic media for stable and tunable spin-dependent optical devices, paving the way for precision sensing and quantum photonic applications.

In **Figure** 8a, we plot the photonic SHE versus the van der Waals (vdW) interaction shift, denoted by $s(r)$, considering a control field strength of $\Omega_c = 5\gamma$. The graph shows that the photonic SHE initially has a positive value when the vdW shift is approximately zero, reaching a maximum magnitude of around 25 λ. As the van der Waals interaction strength increases, the amplitude of the photonic SHE gradually decreases. Upon further increase

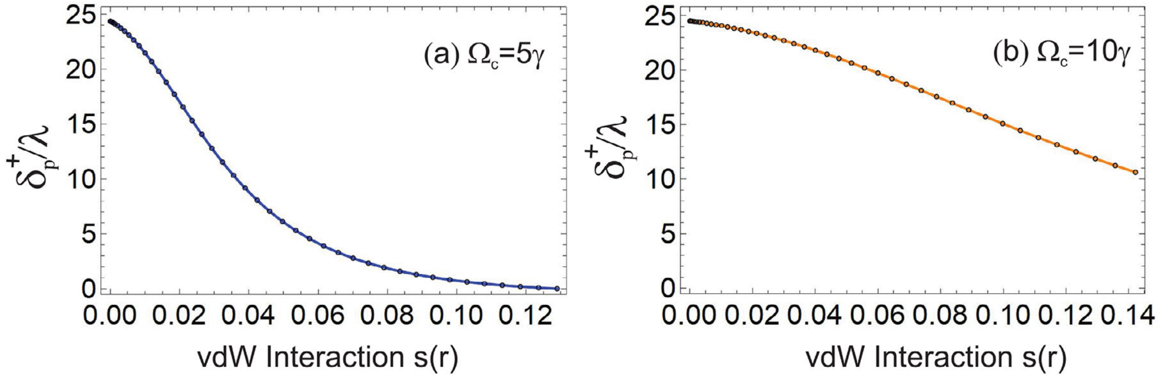

Figure 8. Variation of the photonic SHE with respect to the van der Waals interaction strength $s(r)$. In panel (a), the system is driven by a control field of amplitude $\Omega_c = 5\gamma$, while panel (b) corresponds to an enhanced control field, $\Omega_c = 10\gamma$. Throughout both cases, the atomic number density is fixed at $\mathcal{N} = 10^{12}$ cm^{-3}, and the angle of incidence is maintained at $\theta_i \approx 33.8237°$. Additional parameters include a decay rate $\gamma = 1$ MHz, superatom number $n_{SA} = 20$, near-resonant conditions $\Delta_p = \Delta_c \approx 0$, relaxation rates $\gamma_{eg} = 3\gamma$ and $\gamma_{rg} = 0.01\gamma$, background dielectric constants $\epsilon_1 = \epsilon_3 = 2.22$, probe wavelength $\lambda = 780$ nm, thickness of the intracavity medium $q = 0.5$ µm, and a Gaussian beam waist of $\omega_0 = 50\ \lambda$.

in the vdW shift, the photonic SHE magnitude continues to decline and eventually approaches zero, becoming exactly zero at a vdW shift value of approximately 0.134228.

This behavior can be understood by considering the role of spin-orbit coupling and the dispersion properties induced by the control field in the atomic Rydberg system. At small vdW shifts, the energy levels are only slightly perturbed, allowing strong spin-dependent splitting of optical modes, which enhances the photonic SHE. As the vdW shift increases, interaction-induced modifications to the energy levels reduce the strength of spin-orbit coupling, thereby diminishing the transverse spin-dependent deflection responsible for the photonic SHE. Eventually, at a critical value of the vdW shift ($s(r) \approx 0.134228$), the spin-orbit coupling effect is effectively canceled, leading to the vanishing of the photonic SHE. This represents a balance point where the perturbation due to van der Waals forces neutralizes the spin-dependent optical response induced by the control field.

Furthermore, in Figure 8b, we analyze the behavior of the photonic SHE when the control field strength is increased, i.e., $\Omega_c = 10\gamma$. The graph again shows that the photonic SHE initially has a positive value when the vdW shift is close to zero, achieving a maximum photonic SHE magnitude of 25 λ. As the van der Waals interaction increases, the photonic SHE decreases; however, the reduction is less pronounced compared to the case with a lower control field strength.

When the vdW shift is near zero, the photonic SHE shows a positive value as observed previously, reaching its maximum at this point. This maximum can be attributed to optimal coupling between the probe beam and the material, where the intrinsic material properties (such as polarization and spin-orbit coupling) dominate. The strong positive shift of 25 λ indicates a robust light-matter coupling.

As the van der Waals interaction increases, the photonic SHE gradually decreases. However, due to the stronger control field, the reduction is less severe. The enhanced control field strength boosts the interaction between light and matter, making the system more resilient to the effects of van der Waals interactions. In other words, the system becomes less sensitive to the vdW shift, leading to a smaller reduction in photonic SHE as $s(r)$ increases.

Even as the vdW shift becomes large, the photonic SHE remains non-zero, maintaining a finite value even at $s(r) \approx 0.134228$. This behavior indicates that the stronger control field effectively mitigates the suppressive influence of van der Waals interactions on the photonic SHE. The control field sustains the system's ability to generate a photonic SHE, even under significant vdW perturbations.

While our study addresses the steady-state response under continuous-wave (CW) probe excitation, the presented formalism can be extended to time-dependent or pulsed regimes by retaining the full time derivatives in the Heisenberg-Langevin equations [see Equation (9)]. In such cases, the coherence terms and Rydberg population become time-dependent, allowing exploration of transient dynamics, pulse reshaping, and blockade-induced nonlinear propagation effects. This extension is particularly relevant for investigating phenomena such as slow light and photon storage in strongly interacting Rydberg media, and can be pursued numerically using established methods for solving open quantum system dynamics.

3.1. Experimental Feasibility

The proposed model is experimentally accessible with current technology using ultracold ^{87}Rb atoms. The parameters selected for our simulations such as control and probe Rabi frequencies, atomic densities, decoherence rates, and Rydberg principal quantum numbers are within the range of those used in existing cold-atom experiments involving Rydberg EIT.[32,33] Superatom-based blockade dynamics have been widely observed, and the required optical configurations for observing the photonic SHE can be implemented using standard polarization-sensitive detection methods and cavity-enhanced setups. These considerations suggest that our theoretical predictions could be verified under realistic laboratory conditions.

4. Conclusion

In conclusion, we have theoretically explored the amplification of the photonic SHE in a cavity quantum electrodynamics system incorporating a Rydberg SA medium. Our results demonstrate that the transverse spatial shift exhibits a pronounced peak near the resonance angle, which is directly influenced by the refractive part of the susceptibility of the Rydberg atomic medium. Furthermore, we established that both the magnitude and direction of the transverse displacement, along with the peak position, can be precisely controlled by tuning the system between the resonant and off-resonant detuning regimes. Further, we analyze that the atomic density plays a pivotal role in modulating the photonic SHE, with higher densities enhancing the sensitivity to probe parameters due to strong dipole–dipole interactions, while lower densities yield a more uniform and robust photonic SHE response ideal for stable photonic applications. Moreover, our analysis reveals that the photonic SHE is highly sensitive to the vdW interaction shift, exhibiting maximal transverse displacement at a minimal shift and diminishing with increasing interaction strength, with the suppression mitigated under stronger control fields.

The primary advantage of this approach lies in the strong and tunable photonic SHE, which stems from the intrinsic nonlinear interactions of the Rydberg EIT configuration. This enhanced response, facilitated by the dipole blockade mechanism, renders the system more efficient and versatile compared to linear optical counterparts. Our findings open new avenues for the utilization of Rydberg-based atomic media in advanced photonic applications, including precision metrology, quantum information processing, and spin-controlled photonic devices. Future studies could extend this work to experimental validation and further optimization of the system parameters to maximize control over spin-dependent light-matter interactions.

Acknowledgements

This work was supported by the National Natural Science Foundation of China (Grant No. 12174301), the Natural Science Basic Research Program of Shaanxi (Program No. 2023-JC-JQ-01), and the Fundamental Research Funds for the Central Universities. Hamid R. Hamedi gratefully acknowledges the support from the Research Council of Lithuania (LMTLT), under Agreement No. S-ITP-24-6.

Conflict of Interest

The authors declare no conflict of interest.

Data Availability Statement

Data sharing not applicable to this article as no datasets were generated or analyzed during the current study.

Keywords

electromagnetically induced transparency, photonic spin hall effect, rydberg atoms

Received: May 8, 2025
Revised: August 4, 2025
Published online:

[1] M. Onoda, S. Murakami, N. Nagaosa, *Phys. Rev. Lett.* **2004**, *93*, 083901.
[2] K. Y. Bliokh, F. J. Rodríguez-Fortuño, F. Nori, A. V. Zayats, *Nat. Photonics* **2015**, *9*, 796.
[3] K. Y. Bliokh, Y. P. Bliokh, *Phys. Rev. Lett.* **2006**, *96*, 073903.
[4] J. Sinova, S. O. Valenzuela, J. Wunderlich, C. Back, T. Jungwirth, *Rev. Mod. Phys.* **2015**, *87*, 1213.
[5] S. O. Valenzuela, M. Tinkham, *Nature* **2006**, *442*, 176.
[6] O. Hosten, P. Kwiat, *Science* **2008**, *319*, 787.
[7] F. Cardano, L. Marrucci, *Nat. Photonics* **2015**, *9*, 776.
[8] K. Y. Bliokh, F. J. Rodríguez-Fortu no, F. Nori, A. V. Zayats, *Nat. Photonics* **2015**, *9*, 796.
[9] L. Cai, M. Liu, S. Chen, Y. Liu, W. Shu, H. Luo, S. Wen, *Phys. Rev. A* **2017**, *95*, 013809.
[10] S. Chen, X. Zhou, C. Mi, H. Luo, S. Wen, *Phys. Rev. A* **2015**, *91*, 062105.
[11] A. Aiello, N. Lindlein, C. Marquardt, G. Leuchs, *Phys. Rev. Lett.* **2009**, *103*, 100401.
[12] X. Yin, Z. Ye, J. Rho, Y. Wang, X. Zhang, *Science* **2013**, *339*, 1405.
[13] P. Dong, J. Xu, J. Cheng, *Phys. Plasmas* **2024**, *31*, 1.
[14] D. Petrosyan, J. Otterbach, M. Fleischhauer, *Phys. Rev. Lett.* **2011**, *107*, 213601.
[15] M. D. Lukin, M. Fleischhauer, R. Cote, L. M. Duan, D. Jaksch, J. I. Cirac, P. Zoller, *Phys. Rev. Lett.* **2001**, *87*, 037901.
[16] D. Jaksch, J. I. Cirac, P. Zoller, S. L. Rolston, R. Côté, M. D. Lukin, *Phys. Rev. Lett.* **2000**, *85*, 2208.
[17] E. Urban, T. A. Johnson, T. Henage, L. Isenhower, D. Yavuz, T. Walker, M. Saffman, *Nat. Phys.* **2009**, *5*, 110.
[18] T. Vogt, M. Viteau, J. Zhao, A. Chotia, D. Comparat, P. Pillet, *Phys. Rev. Lett.* **2006**, *97*, 083003.
[19] J. Honer, R. Löw, H. Weimer, T. Pfau, H. P. Büchler, *Phys. Rev. Lett.* **2011**, *107*, 093601.
[20] J.-F. Huang, J.-Q. Liao, C. P. Sun, *Phys. Rev. A* **2013**, *87*, 023822.
[21] Y.-M. Liu, D. Yan, X.-D. Tian, C.-L. Cui, J.-H. Wu, *Phys. Rev. A* **2014**, *89*, 033839.
[22] A. Carmele, B. Vogell, K. Stannigel, P. Zoller, *New J. Phys.* **2014**, *16*, 063042.
[23] R.-G. Wan, M. S. Zubairy, *Phys. Rev. A* **2020**, *101*, 033837.
[24] J. Wu, J. Zhang, S. Zhu, G. S. Agarwal, *Opt. Lett.* **2019**, *45*, 149.
[25] M. Waseem, M. Shah, G. Xianlong, *Phys. Rev. A* **2024**, *110*, 033104.
[26] M. Abbas, Y. Wang, F. Wang, H. R. Hamedi, P. Zhang, *Chaos Solitons Fractals* **2025**, *196*, 116292.
[27] M. Abbas, P. Zhang, H. R. Hamedi, *Phys. Rev. A* **2025**, *111*, 043708.
[28] X.-J. Tan, X.-S. Zhu, *Opt. Lett.* **2016**, *41*, 2478.
[29] L. Wu, H.-S. Chu, W. S. Koh, E.-P. Li, *Opt. Express* **2010**, *18*, 14395.
[30] Y. Xiang, X. Jiang, Q. You, J. Guo, X. Dai, *Photonics Res.* **2017**, *5*, 467.
[31] L. Wu, H. S. Chu, W. S. Koh, E. P. Li, *Opt. Express* **2010**, *18*, 14395.
[32] D. Petrosyan, J. Otterbach, M. Fleischhauer, *Phys. Rev. Lett.* **2011**, *107*, 213601.
[33] J. D. Pritchard, D. Maxwell, A. Gauguet, K. J. Weatherill, M. P. A. Jones, C. S. Adams, *Phys. Rev. Lett.* **2010**, *105*, 193603.